Nuclear Inst. and Methods in Physics Research, A 1016 (2021) 165776

Contents lists available at ScienceDirect

Nuclear Inst. and Methods in Physics Research, A

journal homepage: www.elsevier.com/locate/nima

# Collimating/focusing optical system designed for hard X-ray communication

Yiyang Wang [a], Yunpeng Liu [a,b,*], Junxu Mu [a], Zhaopeng Feng [a], Xiaobin Tang [a,b,**]

[a] Department of Nuclear Science and Technology, Nanjing University of Aeronautics and Astronautics, Nanjing 210016, China
[b] Key Laboratory of Nuclear Technology Application and Radiation Protection in Astronautics, Ministry of Industry and Information Technology, Nanjing 210016, China

ARTICLE INFO

*Keywords:*
Hard X-ray communication, X-ray optics, Collimating/focusing, Supermirror

ABSTRACT

A collimating/focusing (C/F) optical system could greatly reduce the power requirements and improve the communication performance in space communication. Based on the known X-ray source, this paper proposed a hard X-ray multilayer collimating/focusing optical system for X-ray communication (XCOM) in 10–30 keV region. The C/F optical system helps effectively realize XCOM with high gain and high signal to noise ratio (SNR) hundreds of kilometers away. This paper discusses the reflectivity of multilayers, the optimization of supermirrors, the design of C/F optical system for hard X-ray, and the ray tracing process. Results shows that the collection efficiency of hard X-ray is greatly improved, and still remains 0.0196% 1000 km away from the X-ray source. When the transmitting power of X-ray is 100 W, the SNR reaches 71.8 dB at 100 km and 50.1 dB at 1000 km, respectively. This work provides some theoretical and actual values for improving the practical application of X-ray communication in entry blackout and space exploration.

## 1. Introduction

The intense friction between spacecraft and atmosphere will create a plasma sheath on the surface of spacecraft during reentry. In this situation, the radio frequency signal can hardly penetrate the plasma sheath because of its low frequency. This phenomenon is called 'communication blackout', which seriously affects the trajectory control of the spacecraft during landing or reentry. The frequency of X-ray is as high as more than $10^{17}$–$10^{18}$ Hz. With X-ray as carrier, the X-ray communication (XCOM) proposed in 2007 by Dr. Keith Gendreau of NASA is considered a novel method to solve the problem of reentry blackout with the help of the uplink communication. Our previous study indicates that the transmission coefficient of X-ray in plasma sheath is over 0.994 due to plasma channel effect [1]. Moreover, X-ray photons with energies above 10 keV could propagate the distance of 1000 parsec with almost no loss, that means X-ray can be utilized as a carrier in interstellar communication [2].

However, the practical applications of current XCOM technology still have several limitations. For instance, the large divergence angle (near $2\pi$) for the transmitter, called modulated X-ray source, cannot support long distance communication because of the huge geometrical attenuation. Furthermore, XCOM has high requirements for the transmission power of hard X-ray sources as well as the sensitivity and collection efficiency of X-ray detectors. The trajectory of X-ray with energy over 10 keV is difficult to be changed because of its high frequency. In this case, an effective X-ray collimating/focusing (C/F) optical system can greatly reduce the divergence loss of X-ray in long-distance transmission, increase the collection efficiency of the X-ray detector, and realize effective communication in blackout area.

Many structures are proposed to reflect X-ray, such as poly-capillary X-ray lens, lobster eye X-ray telescope, Wolter mirrors, and K–B micro-focusing system. The nested Wolter soft X-ray telescope was built in NASA's NICER mission launched in 2017 [3,4]. The new Japanese X-ray Astronomy satellite Hitomi (ASTRO-H) was launched on HII-A, Japan's primary large vehicle on February 17, 2016 [5–8]. A nested conical focusing telescope with a single layer was designed for pulsar signals in soft X-ray by Xi'an Institute of Optics and Precision Mechanics of CAS [9]. The most recent large mission of the X-ray telescope is the Athena telescope in Europe, which is scheduled to be launched in 2028 [10]. Coating on the substrate can improve the reflectivity of X-ray and enlarge the critical grazing incidence angle. The supermirror proposed by Mezei is a type of periodic multilayers used in neutron optics, which was extended to the X-ray region by Joensen et al. later in 1992 [11–13]. This scheme can improve the reflectivity of hard X-ray significantly. Nesting several reflectors made by supermirrors is helpful to reduce the volume and improve the area utilization in hard X-ray C/F optical system [14]. However, the current X-ray telescopes are mainly used for pulsar navigation and astronomical detection, which cannot be directly used for XCOM because of the differences in energy range. In this case, it is urgent to design a complete C/F optical system specially designed for hard X-ray communication.

* Corresponding author at: Department of Nuclear Science and Technology, Nanjing University of Aeronautics and Astronautics, Nanjing 210016, China.
** Corresponding author.
*E-mail addresses:* liuyp@nuaa.edu.cn (Y. Liu), tangxiaobin@nuaa.edu.cn (X. Tang).

https://doi.org/10.1016/j.nima.2021.165776
Received 19 June 2021; Received in revised form 1 September 2021; Accepted 2 September 2021
Available online 5 September 2021

This paper proposes the scheme of a hard X-ray collimating/focusing optical system composed of nested confocal conical supermirrors. The system is aimed to increase the reflectivity of hard X-ray, reduce the divergence angle of X-ray, lower the power requirements of X-ray sources, and enlarge the communication distance in hard X-ray communication.

## 2. Theories and methods

### 2.1. Parameters of X-ray source

To communicate in entry blackout by using hard X-ray, the X-ray source should emit pulsed X-ray photons with energy over 10 keV, small divergence angle, and high intensity. Therefore, a W-target X-ray source with a 50 kV tube voltage is used in this study, and it can emit X-ray with energy range of 0–50 keV. The energy of X-ray generated by the X-ray source used in this study is mainly concentrated in the range of 0–30 keV, but X-ray with energy lower than 10 keV cannot penetrate the plasma sheath effectively. Therefore, only X-ray in 10–30 keV are considered in this study [15,16]. The energy spectrum and the X-ray distribution curve flux of the X-ray source is shown in Fig. 1. In the subsequent simulation, the "source radial" is used to simulate the X-ray source. Through this type of source, the energy spectrum and self-defined distribution curve flux of the X-ray source can be set, so that the simulation results would be closer to the real situation.

### 2.2. Reflectance of multilayers

In X-ray region, the absorption of the interaction between X-ray and matter cannot be ignored. Thus, the refractive index is expressed in complex form as follows:

$$\tilde{n} = 1 - \alpha - i\beta, \tag{1}$$

where $\alpha$ represents the refraction characteristics of X-ray, and $\beta$ is the extinction coefficient, which represents the absorption characteristics of photons. $\alpha$ and $\beta$ in Eq. (1) should be given as

$$\alpha = \frac{N_A \rho r_e \lambda^2}{2\pi M} f_1(E), \tag{2}$$

$$\beta = \frac{N_A \rho r_e \lambda^2}{2\pi M} f_2(E), \tag{3}$$

where $N_A$ is the Avogadro constant, $r_e$ represents the classical electron radius, $\rho$ is the material density, $\lambda$ is the wavelength of incident X-ray photons, $M$ is the molecular weight of elements, and $f_1$ and $f_2$ are the scattering factors of elements respectively, which are given by Henke tables.

The Fresnel reflection coefficient of a single-layer can be obtained by solving the Fresnel equation with the reflection law and Snell's law [17]

$$r_j = \frac{\cos\theta - \tilde{n}_j \cos\theta_j}{\cos\theta + \tilde{n}_j \cos\theta_j} \text{ (s)}, \tag{4}$$

$$r_j = \frac{\tilde{n}_j \cos\theta - \cos\theta_j}{\tilde{n}_j \cos\theta + \cos\theta_j} \text{ (p)}, \tag{5}$$

The reflectivity of multilayers is usually obtained by iteration: if isotropic uniform layers with a thickness of $d_j$ and complex refractive index of $\tilde{n}_j = 1 - \alpha_j - i\beta_j$ are coated on the substrate with complex refractive index of $\tilde{n}_0 = 1 - \alpha_0 - i\beta_0$, the complex amplitude reflectance can be given by Berning equation, when the monochromatic parallel light with a wavelength of $\lambda$ incidents on the surface of the multilayers at an angle of $\theta$ [17]

$$R_j = \frac{r_j\left(1 - r_j R_{j-1}\right) + \left(R_{j-1} - r_j\right)\exp(-i\delta_j)}{1 - r_j R_{j-1} + r_j\left(R_{j-1} - r_j\right)\exp(-i\delta_j)}, \tag{6}$$

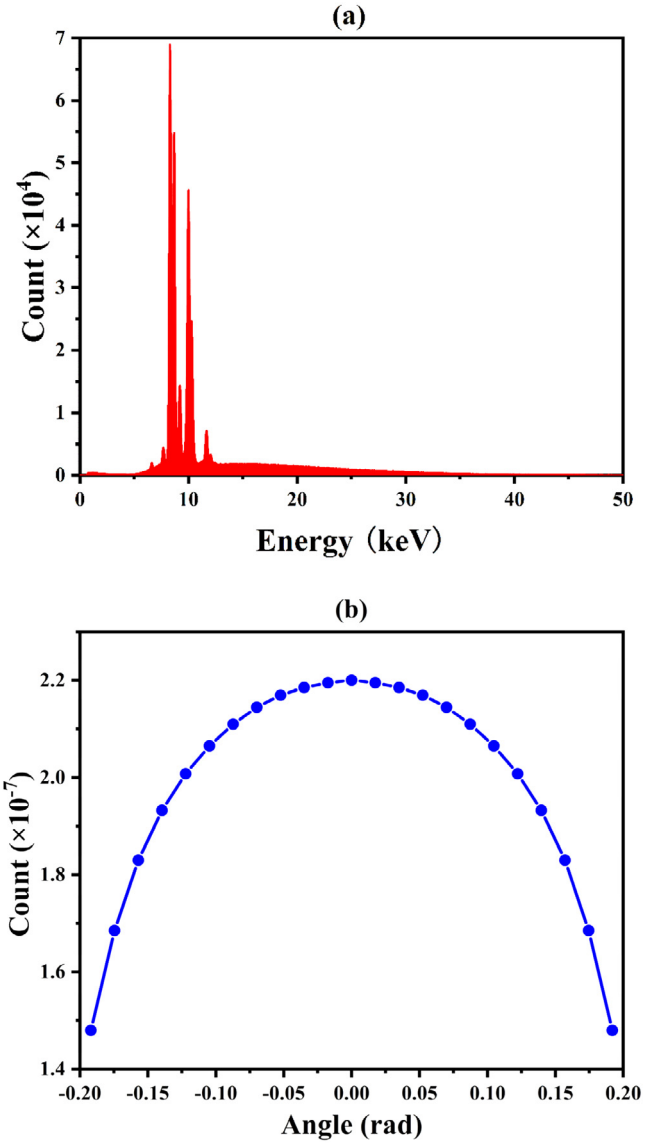


**Fig. 1.** (a) Energy spectrum of X-ray source with W-target under a 50 kV tube voltage. X-ray with energy between 10 and 30 keV are used. (b) Intensity of X-ray at different angles. More than 80% of the X-ray emitted by the X-ray source are concentrated within 0.20 rad.

$$\delta_j = \frac{4\pi\tilde{n}_j d_j \cos\theta_j}{\lambda}, \tag{7}$$

where $R_j$ and $R_{j-1}$ are the total amplitude reflectance of the multilayers after the $j$th and ($j$-1)th layers, respectively. The term of $r_j$ is the Fresnel reflection coefficient of the $j$th layer material, and $\delta_j$ is the phase difference.

Two roughness models are introduced to modify the Fresnel reflection coefficient [18,19].

$$r_j^* = r_0 \frac{8\pi^2\sigma^2 \exp(-n_1 n_2 \cos\theta_1 \cos\theta_2)}{\lambda^2} \text{ (Debye–Waller factor)}, \tag{8}$$

$$r_j^* = r_0 \exp\left(\frac{8\pi^2\sigma^2\sqrt{n_1^2 - n_0^2\sin\theta_i^2}\sqrt{n_2^2 - n_0^2\sin\theta_i^2}}{\lambda^2}\right) \text{ (Nevot–Croce factor)}, \tag{9}$$

where $r_j^*$ is the modified Fresnel reflection coefficient, $r_0 r_0$ is the uncorrected Fresnel reflection coefficient, $\sigma$ is the roughness coefficient ($\sigma$ = 0.5 nm in this paper), $n_1$ and $n_2$ are the refractive indices of the

scattering W layer and the absorbing $SiO_2$ layer, respectively; $\theta_i$ is the grazing incidence angle of X-ray; and $\theta_1$ and $\theta_2$ are the refraction angles of X-ray incident on the W and $SiO_2$ layers, respectively. By making up these two roughness models, the calculated reflectivity is closer to the actual situation.

The selection criteria of the materials are constrained by their optical and physical–chemical properties. The best pairs of materials for X-ray multilayers should display high optical contrast, minimal absorption, non-absorption-edge in the bandwidth of interest, and sharp interfaces with small roughness [20]. According to all these considerations, the $W/SiO_2$ pairs are chosen to be the materials of layers.

To increase the reflectivity, dozens or even hundreds of layers with different materials and thicknesses should be coated on the substrate [21]. Thompson sampling based on Beta distribution is proposed to maximize the reflectivity in this study. Beta distribution refers to a group of continuous probability distributions defined on the interval [0,1] parameterized by two positive shape parameters, denoted by a and b. The properties of beta distribution are as follows:

i. a/(a + b) is the mean value of sampling. The larger it is, the closer the center of probability density distribution is to 1. Most of the random numbers generated by this probability distribution are close to 1, otherwise they are close to 0.
ii. larger (a + b) leads to narrower distribution and higher concentration. Thus, the random number produced is closer to the center position, which can be observed from the variance formula.

With this property of Beta distribution, Thompson sampling will try a variety of different schemes through a large number of samplings, and evaluate these schemes through certain evaluation methods. The best scheme is obtained by sampling, evaluating, and modifying the shape parameters of each scheme.

### 2.3. Design of collimating/focusing optical system

The collimating/focusing optical system consists of many nested supermirrors, called reflectors, in the shape of a cone with a common focus, as shown in Fig. 2. Taking no account of imaging, the cone is chosen to be the shape of reflector because of its simple manufacture and high area utilization. The inner surface of the reflector contains many layers, which forms the supermirror. The trajectory of X-ray changes when it passes through the inner surface of the supermirrors according to the Bragg diffraction law:

$$2d \sin\theta = \lambda, \tag{10}$$

where $d$ is the period thickness and $\theta$ is the grazing incidence angle.

The axial projection length of the collimator is set as 50 mm to meet the requirements of small volume and light weight. The divergence angle of X-ray emitted from the X-ray source is $\theta_0$, but the X-ray collimator can only change the trajectory of X-ray within $\theta^*$, which means the distance $D$ from the middle point of the reflector to the X-ray source affects the energy received by the collimator. The distance $D$ is set as 2000 mm in this paper.

The relationship between the entrance radius of the collimator and the distance $D$ can be written in the following form:

$$R_{in} = \frac{2Dk_i}{1-{k_i}^2} - \frac{1}{2}Lk_i, \tag{11}$$

where $R_{in}$ is the entrance radius of the outermost layer of the reflector, $D$ is the distance from the point in the reflector to the X-ray source, $L$ is the axial projection length of the reflector, and $k_i$ is the slope of the reflector.

The slope of each reflector and the inner radius of the entrance and exit are given as

$$k_i = \frac{R_{out\_i} - R_{in\_i}}{L}, \tag{12}$$

$$\frac{2Dk_i}{1-{k_i}^2} = \frac{R_{out\_i} - R_{in\_i}}{2f}, \tag{13}$$

$$R_{out\_(i+1)} = R_{in\_i} - d, \tag{14}$$

where the subscript $i$ represents the $i$th reflector from the outside to the inside; $k_i$ is the slope of the reflector; $R_{out-i}$ and $R_{in-i}$ represent the inner radius of the X-ray exit and the entrance of the reflector, respectively; $L$ is the axial projection length of the reflector, and $f$ is the focal length.

Referring to mature experience [3–8], the focal length of the X-ray concentrator $F_f$ is set as 8000 mm, the axial length of the reflector is 300 mm, and the thickness of reflector is 0.3 mm. Under those conditions, the slope of each reflector and the inner radius of the entrance and exit are still given by Eqs. (12), (13) and (14).

The optimal entrance radius of the X-ray concentrator is determined by the effective collection area, which is the sum of the product of the area of the projection circle of each layer of the reflector on the focal plane and the reflectivity of the layer.

Considering the structural strength of the whole device, we set four mutually perpendicular ribs in the C/F optical system. The outermost and innermost ends of the four ribs installed in the collimator is 5 mm and 1 mm wide, respectively. The outermost and innermost ends of the four ribs installed in the concentrator is 10 mm and 1 mm wide, respectively. Demonstration of the collimating/focusing optical system is shown in Fig. 2.

### 2.4. Ray tracing method

After the structure of the C/F optical system is determined, settings in the simulation need to be explained. In the whole simulation process, all surfaces perpendicular to the axial direction of the X-ray source in the C/F optical system are set as "absorption", that means, the X-rays will not be tracked after entering these planes. The inner surfaces of all nested layers are set as both "reflection" and "scattering", because these inner surfaces are coated to change the X-ray transmission path. The outer surface of the nested layers is set as "absorption", which is to reduce the influence of stray rays in the simulation process as well as the required simulation time. Then some counting planes with different areas are set up to count X-rays. The interaction process between X-ray and collimator is shown in Fig. 3.

The complete process of ray tracing is:

i. Rays start at the source and transmit in vacuum;
ii. Rays hit a surface and change direction due to reflection or refraction;
iii. When the rays do not encounter an object or a counting surface, the ray tracing is over.

As Fig. 3 shows, the starting position ($P_s$) with the coordinates ($x_s$, $y_s$, $z_s$) of the X-ray beam is sampled uniformly in the source area. According to the energy spectrum in Fig. 1(a), the energy ($E_s$) of the X-ray beam is sampled. The direction of the X-ray beam is expressed as $\overrightarrow{u_c}$. We obtain $\overrightarrow{u_c}$ by sampling two angle parameters $\theta_{xy}$ and $\theta_z$ according to the X-ray distribution curve flux in Fig. 1(b):

$$\overrightarrow{u_c} = \left(\cos\theta_{xy}\sin\theta_z, \sin\theta_{xy}\sin\theta_z, \cos\theta_z\right) \tag{15}$$

Therefore, the ray trajectory equation is:

$$\frac{x-x_s}{u_{c\_x}} = \frac{y-y_s}{u_{c\_y}} = \frac{z-z_s}{u_{c\_z}} \tag{16}$$

Then, the inner surface of the reflector labeled $n$ in the collimator is described as:

$$F_{c\_n}(x,y,z) = \frac{(z-z_c)}{L} - \frac{\sqrt{x^2+y^2} - R_{in\_i}}{R_{out\_i} - R_{in\_i}} \tag{17}$$

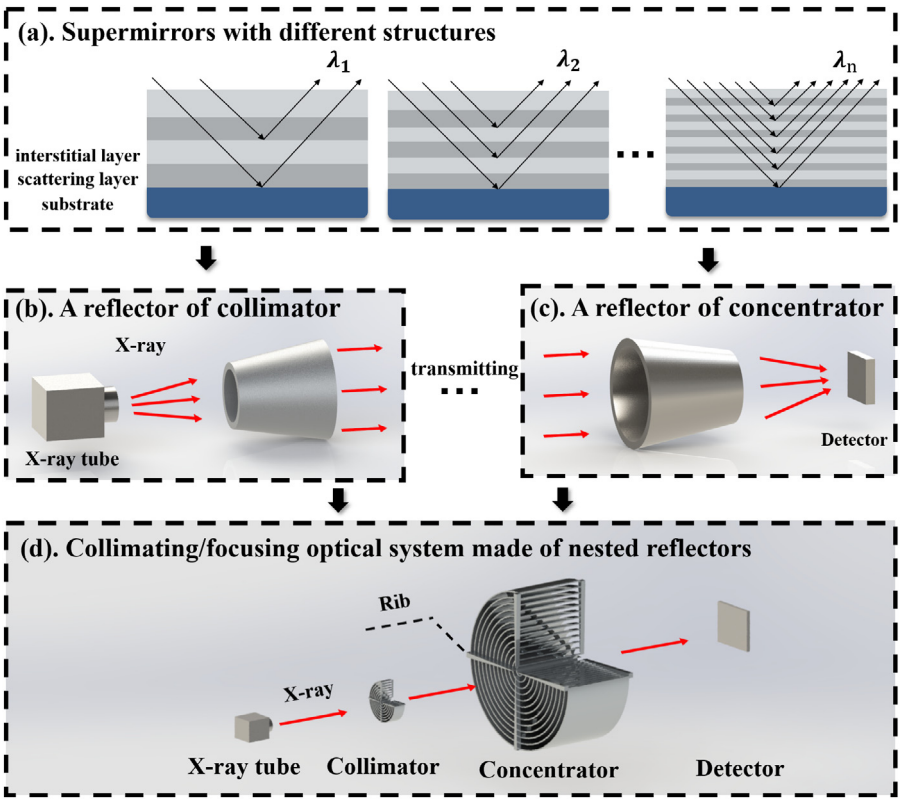


**Fig. 2.** Structure diagram of the C/F optical system. Firstly, (a) different supermirrors are customized for X-ray with different wavelengths; and then the reflectors of (b) collimator and (c) concentrator made by supermirrors are designed, respectively; finally, all these reflectors constitute (d) the complete C/F optical system.

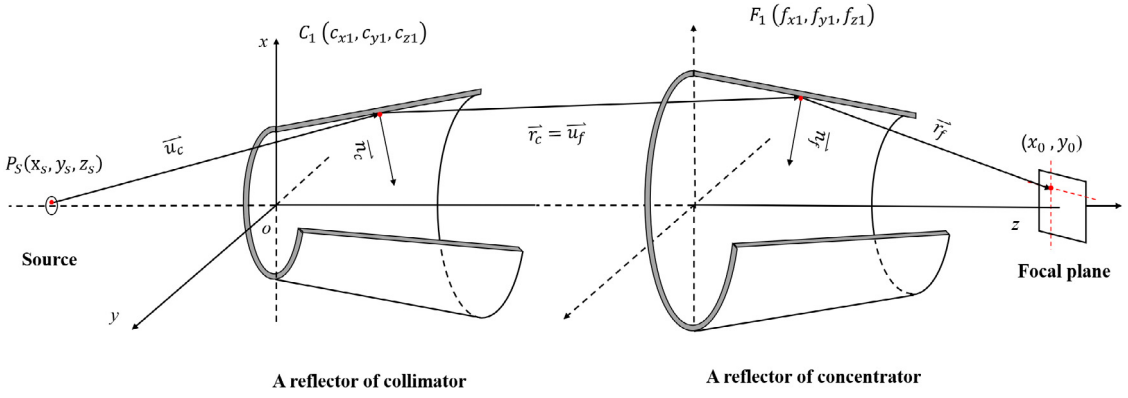


**Fig. 3.** Diagram of X-ray transmission in the collimator.

And its surface normal vector is:

$$\overrightarrow{n_c} = \left(\frac{\partial F_{c_i}}{\partial x}, \frac{\partial F_{c_i}}{\partial y}, \frac{\partial F_{c_i}}{\partial z}\right) = \left(-2x, -2y, \frac{2\left(R_{out\_i} - R_{in\_i}\right)}{L} \times \left[\frac{(z - z_{pc})(R_{out\_i} - R_{in\_i})}{L} - R_{in\_i}\right]\right) \tag{18}$$

Substitute Eq. (16) into Eq. (17) above, the coordinates of the intersection can be written as $C_1\ (c_{x1}, c_{y1}, c_{z1})$, and Eq. (17) becomes:

$$F_{c\_n}(x, y, z) = \frac{(z - z_{pc})}{L} - \frac{\sqrt{\left[x_s + \frac{u_x}{u_z}(z - z_s)\right]^2 + \left[y_s + \frac{u_y}{u_z}(z - z_s)\right]^2} - R_{in\_i}}{R_{out\_i} - R_{in\_i}} \tag{19}$$

It is important to note that if the X-ray beam collides with the surfaces perpendicular to Z axis (marked as shadow in Fig. 3), it will be discarded, which means only the X-ray beams which collide with the inner surface of reflector will be considered.

Then the reflection vector $\overrightarrow{r_c}$ can be given as:

$$\overrightarrow{r_c} = \overrightarrow{u_c} - 2\overrightarrow{n_c}\sin\theta \tag{20}$$

$$\sin\theta = \overrightarrow{u_c} \cdot \overrightarrow{n_c} \tag{21}$$

where $\theta$ is the angle between the incident vector and the reflector of the collimator, that is the grazing incidence angle. The reflectivity of X-rays in the collision is given in Fig. 4 with the method in Section 2.2. After the X-ray beam collides with the inner surface of the collimator, it will propagate along the direction of $\overrightarrow{r_c}$. At this time, it is necessary to calculate the intersection $C_2\ (c_{x2}, c_{y2}, c_{z2})$ between the outer surface of the inner reflector of the collimator and $\overrightarrow{r_c}$. If $c_{z2} \le L$, which means the X-ray beam collides with the outer surface of the inner reflector and is absorbed, this X-ray beam will be discarded. Otherwise, the X-ray beam will continue to propagate until the position of the concentrator.

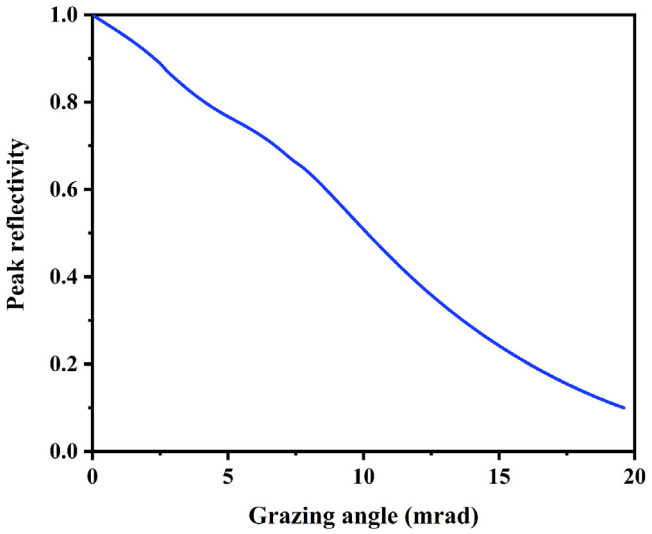


**Fig. 4.** Peak reflectivity of X-ray with different grazing angle.

Taking the reflection vector $\overrightarrow{r_c}$ as the incident vector $\overrightarrow{u_f}$ of the concentrator, the trajectory and coordinates of the interaction between X-ray and the concentrator are obtained in the same way like the collimator. The coordinates, energy and other parameters of the X-ray are recorded in the focal plane, so as to obtain the spatial distribution of intensity. By using the ray tracing method to obtain trajectories of the X-ray beam and determine whether it could reach the focal plane, the flux of the beam at the entrance and the focal plane of the C/F optical system will be obtained. The transmission efficiency is calculated by the flux parameters [22]:

$$\eta = \frac{I_f}{I_0} \tag{22}$$

where $\eta$ is the transmission efficiency of the C/F optical system, $I_f$ is the flux of the focal plane, and $I_0$ is the flux of X-ray source.

## 3. Results and discussion

### 3.1. Peak reflectivity at different incident angles

The specific thickness of each layer can be determined quickly by Thompson sampling. In this method, the reflectivity of each reflector reaches the maximum, and the full width at half maximum (FWHM) of the reflectivity curve is broadened, which makes up for the performance degradation of X-ray off-axis incidence.

For reflectors with different slopes, their multilayers and reflectivity are different. When the incident angle of X-ray photons $\theta$ is larger than 19.6 mrad, coating even hundreds of layers can hardly make the reflectivity over 10%. Therefore, the multilayers are no longer designed when $\theta > 19.6$ mrad. The maximum reflectivity at different grazing angles is shown in Fig. 4.

With those steps above, W and $SiO_2$ layers are alternately sputtered on the substrate according to the optimization results of Thompson sampling. These reflectors are mounted as a confocal nested cone structure, and finally form a complete X-ray collimating/focusing optical system.

### 3.2. Performance of collimator

The length of the collimator is set as $L_c = 50$ mm and the focal length of the collimator is set as $F_c = 2000$ mm. The area utilization, which refers to the ratio of the effective collection area to the maximum cross-sectional area in the space occupied by the collimator, reaches 24.36% when the distance between the X-ray collimator and the X-ray source is 1975 mm. The inner diameter of the entrance of the outermost reflector is 78.0 mm, which is determined by the chosen focal length. With the inner radius of the entrance and the focal length, the other parameters are calculated by Eqs. (12), (13), and (14). Table 1 shows the geometric parameters of the collimator.

**Table 1**
Parameters of collimator.

| Parameter | Value | Unit |
|---|---|---|
| Maximum grazing angle | 19.6 | mrad |
| Maximum outer radius | 79.3 | mm |
| $L_c$ | 50 | mm |
| $F_c$ | 2000 | mm |
| Layers | 113 | – |

**Table 2**
Parameters of concentrator.

| Parameter | Value | Unit |
|---|---|---|
| $L_f$ | 300 | mm |
| $F_f$ | 8000 | mm |
| Layers | 158 | – |
| Maximum radius | 316.2 | mm |
| Maximum grazing angle | 19.55 | mrad |
| Occupied area | $3.141 \times 10^5$ | $mm^2$ |
| Effective collection area | $9.946 \times 10^4$ | $mm^2$ |

After the X-ray source is collimated by the collimator, there is 0.872% of the total X-ray energy being projected on a plane of a circle with a radius of about 317 mm at 100 km away from the source. This value remains 0.0802% 1000 km away in the same case. The collimator imaging results at 100 and 1000 km obtained by ray tracing method in Section 2.4 are shown in Fig. 5 when the transmitting power of the X-ray source is 100 W. X-ray maintains a relatively complete spatial distribution on the incident surface of the focusing device at 100 km in Fig. 5(a). The low counting area caused by the ribs can be observed. The intensity distribution of X-ray is concentrated with the peak width of about 150 mm. As the distance increases to 1000 km, the spatial distribution of X-ray in Fig. 5(b) is no longer complete. The low count area caused by ribs cannot be distinguished. The peak width enlarges to about 1000 mm.

### 3.3. Performance of the collimating/focusing optical system

Under the set conditions of the focal length $F_f = 8000$ mm and the axial length of mirrors $L_f = 300$ mm, the entrance radius of the concentrator can be obtained based on the total effective collection area. The optimum entrance radius is 316.2 mm because the total effective collection area will not increase anymore above that value. With the entrance radius of the focusing device and the focal length and the axial length of reflectors, the parameters of the concentrator are calculated by Eq. (11) and shown in Table 2.

After all those steps, under the condition of the X-ray source used in this paper, the output of the collimator is set as the input of the concentrator.

The energy of X-ray deposited in the focal plane of the concentrator is counted by ray tracing method in Section 2.4. The energy deposited on the square detection area with a side length of 60 mm in the focal plane accounts for 0.274% of the total emission at 100 km. This number still remains 0.024% at 1000 km. The concentrator imaging results at 100 and 1000 km obtained by ray tracing method in Section 2.4 are shown in Fig. 6 when the transmitting power of the X-ray source is 100 W. As shown in Fig. 6(a), a very sharp counting peak appears on the counting area with a side length of 634 mm. When the side length is reduced to 60 mm in Fig. 6(b), the X-ray presents an ideal counting peak, and the low counting region formed by the ribs is also clearly visible. Moreover, the FWHM is 13.0 mm. With the distance increasing

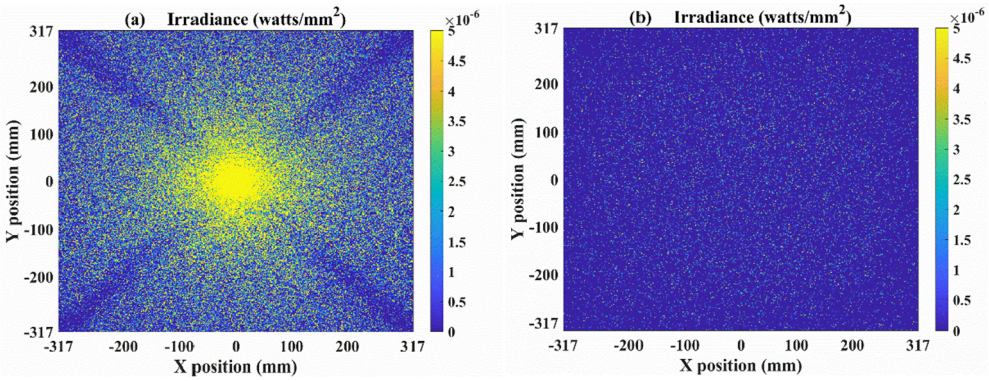


**Fig. 5.** Imaging results of collimator at (a) 100 km and (b) 1000 km.

to 1000 km in Fig. 6(c), the counting peak is not as sharp as before. It can be seen the low counting area formed by ribs is becoming fuzzy and the peak is dispersed in the whole detection area in Fig. 6(d).

As shown in Fig. 7, the irradiance at the receiving terminal decreases continuously with the transmission distance increasing from 1 to 1000 km, but the curve still maintains an obvious peak shape. For the X-ray C/F optical system designed in this scheme, it is basically sufficient for the detection area of 60 mm in diameter to collect most X-ray within 1000 km distance.

Besides, the collection efficiency is essential to evaluate the C/F optical system. This value is the ratio of the received X-rays to the X-rays emitted by the source which is calculated by Eq. (22). Fig. 8 shows the collection efficiency at different transmission distances. The efficiency is fairly low without the collimating/focusing optical system, and it reduces to $1.8\times10^{-6}$ at 1 km. With the help of the concentrator only, the collection efficiency is slightly improved. While the efficiency is increased by more than three orders of magnitude with the collimator only. Coupling both collimator and concentrator, the efficiency is further improved, especially in long transmission distances such as 1000 km. The collimating is the premise of the focusing, and the effect of the focusing becomes more significant with the increase in transmission distance. In addition, the collection efficiency with the collimator is slightly higher than that with both collimator and concentrator at 1 km. This is because that the area of light beam is less than the counting area so that a part of the X-ray is sheltered by the concentrator. We can draw the conclusion that the collimating/focusing optical system effectively expands the transmission distance of the X-ray emitted from the X-ray source.

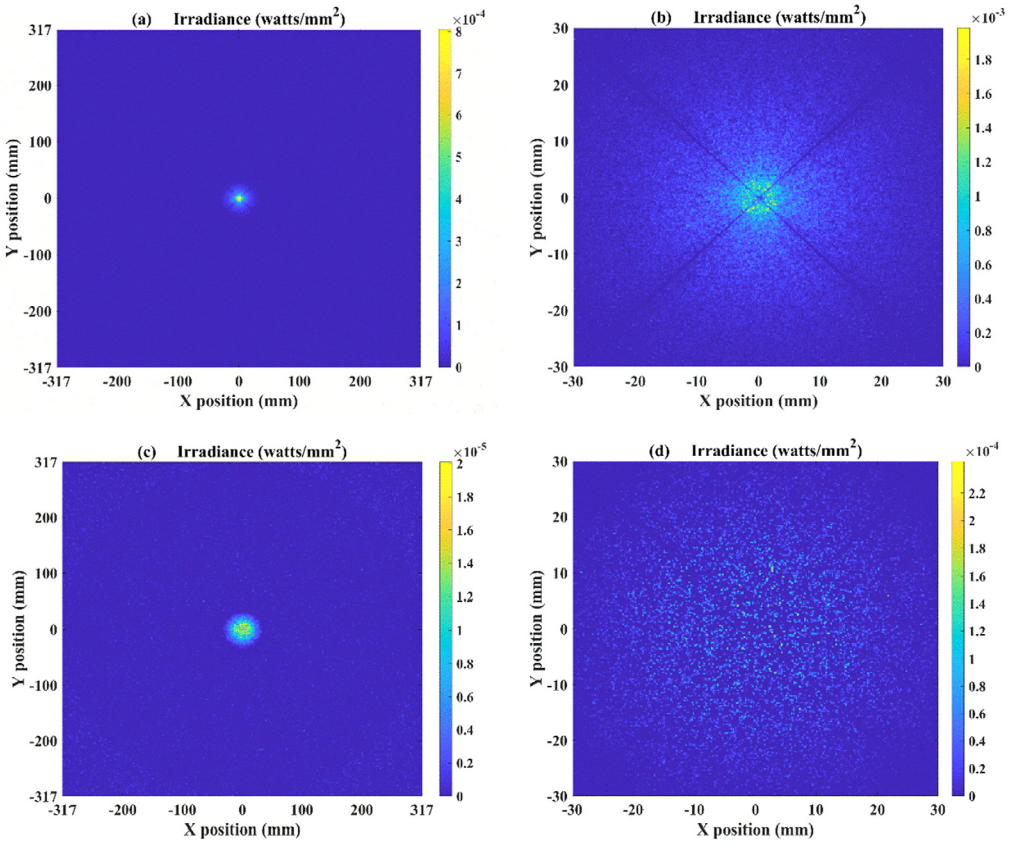


**Fig. 6.** Imaging results of the concentrator which take (a) 634 mm and (b) 60 mm as the side length at 100 km, respectively; and the imaging results of the concentrator which take (c) 634 mm and (d) 60 mm as the side length at 1000 km, respectively.

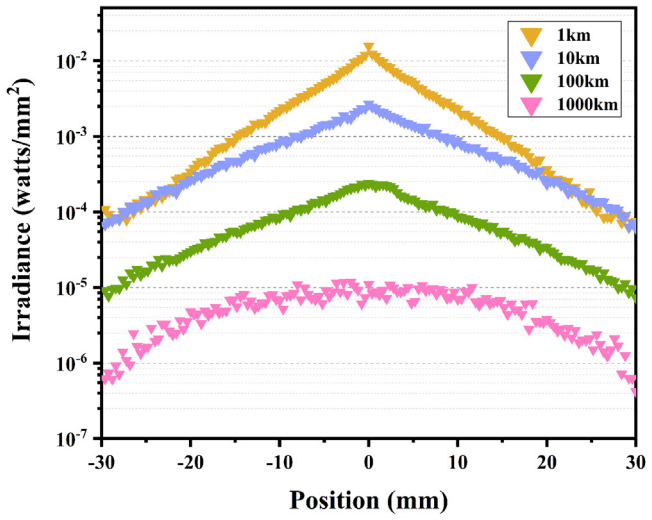


**Fig. 7.** Irradiance curves of the concentrator at different distances. The detection area is a square with a side length of 60 mm in the focal plane.

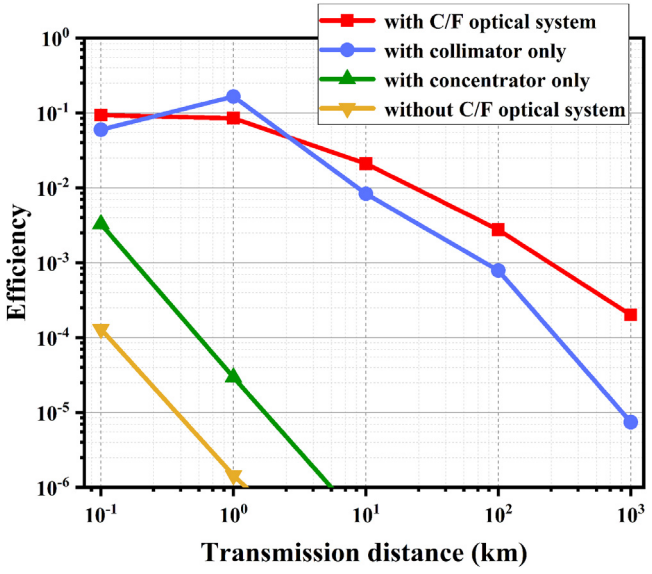


**Fig. 8.** Relationship between collection efficiency and transmission distance.

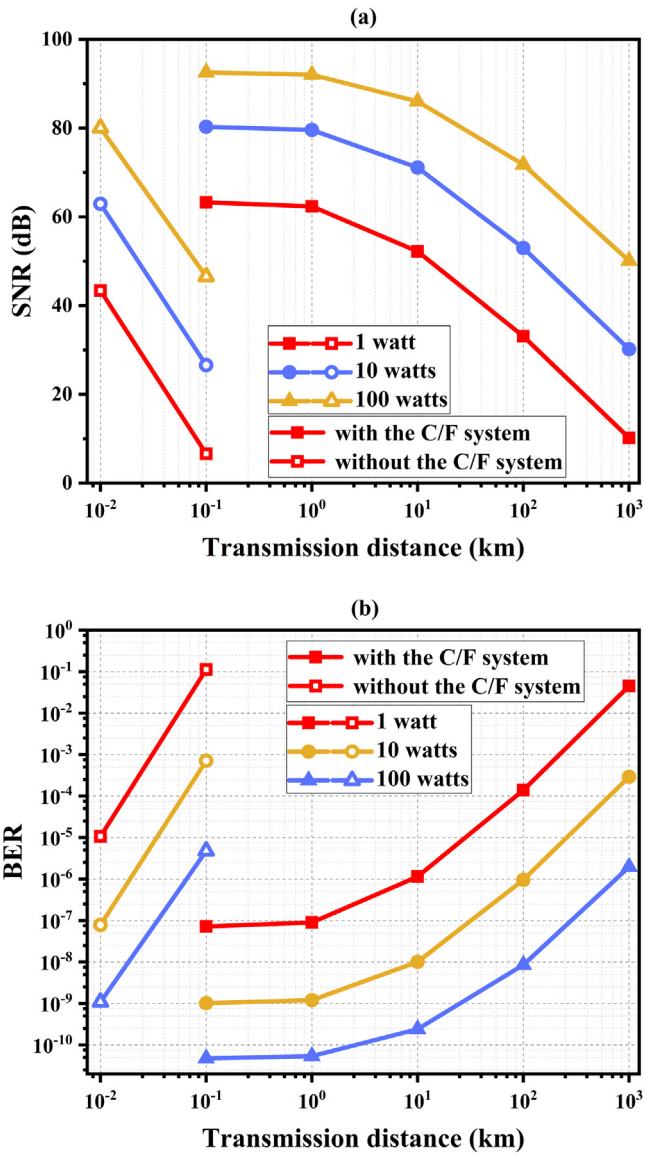


**Fig. 9.** Changes of (a) SNR and (b) BER with transmission distance.

### 3.4. Communication performance

The modulated X-ray emitted by the X-ray source is reflected by the collimator and concentrator successively, and then captured by the CdZnTe (CZT) detector, which generates voltage pulses. After the pulse signal is demodulated, the required information is obtained. This is the complete information transmission process. For the XCOM, X-ray signal is usually modulated by intensity or amplitude, and signal recovery usually adopts envelope detection, which belongs to incoherent detection. Generally, the signal to noise ratio (SNR) is calculated from dark current noise, background noise, thermal noise according to Eq. (23) and the variance is $\sigma_d^2$, $\sigma_{bg}^2$ and $\sigma_{th}^2$, respectively [23]. The dark current of the CZT detector used is 10 nA, the equivalent impedance of electronic circuit is 1000 Ω, and the background noise flow is set as 1 counts/s/keV/m$^2$. The bit-error-rates (BER) is calculated by Eq. (24) according to the Refs. [24,25].

$$SNR = 10\log_{10}\frac{\left(\frac{\eta q}{h\upsilon}P_r\right)^2}{\left(\sigma_{bg}^2+\sigma_d^2+\sigma_{th}^2\right)}\frac{B}{R_{im}} \tag{23}$$

$$BER = 0.25erfc\left(\frac{\sqrt{SNR}}{2}\right)+0.5e^{-\frac{SNR}{4}} \tag{24}$$

As shown in Fig. 9(a), the SNR decreases rapidly with the increase of transmission distance without the C/F optical system. In contrast, the SNR with the C/F optical system reaches 71.78 dB at 100 km, and it remains 50.08 dB at 1000 km, when the transmitting power of the X-ray source is 100 W. As shown in Fig. 9(b), the BER increases as the transmission distance increases. For the designed collimating/focusing optical system, the BER of hard X-ray communication is as low as $8.57\times10^{-9}$ when the transmission distance is 100 km and the power of X-ray source is 100 W. The BER is still less than $1.97\times10^{-6}$ when the distance reaches 1000 km. In the same case, the BER reaches $5.00\times10^{-6}$ 0.1 km away from the X-ray source without the C/F optical system. Therefore, the communication distance with the C/F optical system proposed is greatly extended by at least four orders of magnitude compared with that without the optical system at the same bit error rate.

## 4. Conclusion

A complete collimating/focusing optical system for hard X-ray in 10–30 keV is designed in this paper. The collimator has 113 nested reflectors, the maximum diameter of the collimator entrance is 158.5 mm, and the effective collection area is $4.169 \times 10^3$ mm$^2$. The concentrator has 158 nested reflectors, the maximum diameter of the entrance is 632.4 mm, and the effective collection area is $9.946 \times 10^4$ mm$^2$. The maximum grazing angle of both collimator and concentrator is 19.6 mrad.

The transmission characteristics of the designed C/F optical system is studied with the ray tracing method. With the X-ray C/F optical system participating in X-ray transmission, the collimator projects 0.872% of the energy emitted by the X-ray source, the X-ray concentrator collects 31.45% of them, and 0.274% of the total X-ray energy emitted is deposited on the square detection area with side length of 60 mm at 100 km. Moreover, for the 1000 km distance, they are 0.0802%, 24.4%, and 0.0196%, respectively. The collimating/focusing optical system effectively expands the transmission distance of the X-ray emitted from the X-ray source.

By introducing the C/F optical system into the hard X-ray communication, the SNR reaches 71.8 dB at 100 km and 50.1 dB at 1000 km, respectively, when the transmitting power of X-ray is 100 W. The communication distance with the C/F optical system proposed is greatly extended by at least four orders of magnitude compared with that without the optical system at the same bit error rate. This work provides some theoretical and actual values for improving the practical application of X-ray communication in entry blackout and space exploration.

## CRediT authorship contribution statement

**Yiyang Wang:** Conceptualization, Methodology, Visualization, Data curation, Writing – original draft. **Yunpeng Liu:** Conceptualization, Writing – review & editing. **Junxu Mu:** Writing – review & editing. **Zhaopeng Feng:** Writing – review & editing. **Xiaobin Tang:** Supervision, Writing– review & editing.

## Declaration of competing interest

The authors declare that they have no known competing financial interests or personal relationships that could have appeared to influence the work reported in this paper.

## Acknowledgment

This work was supported by the Aeronautical Science Fund, China (Grant No. 2018ZC52029).

## References

[1] Y. Liu, H. Li, Y. Li, S. Hang, X. Tang, Transmission properties and physical mechanisms of X-ray communication for blackout mitigation during spacecraft reentry, Phys. Plasmas. 24 (2017) 1–9.

[2] S. Hang, X. Tang, H. Li, Y. Liu, J. Mu, W. Zhou, A novel approach for interstellar communication based on modulated X-ray beams, in: The 69th International Astronautical Congress, Bremen, Germany, 2018, pp. 1-5, IAC-18, A4, 1, 8, x43834.

[3] E. Balsamo, K. Gendreau, Z. Arzoumanian, T. Okajima, L. Jalota, Y. Soong, P. Serlemitsos, T. Enoto, B. Gulati, S. Kenyon, D. Hahne, D. Fickau, N. Spartana, S. Lentine, C. Burdhimo, B. Barrios, L. Wu, Concept study x-ray testing for nicer's x-ray concentrators, Opt. EUV, X-Ray, Gamma-Ray Astron. VI 8861 (2013) 88611M.

[4] W.H. Yu, S.R. Semper, J.W. Mitchell, L.B. Winternitz, M.A. Hassouneh, S.R. Price, P.S. Ray, K.S. Wood, K.C. Gendreau, Z. Arzoumanian, NASA SEXTANT mission operations architecture, Acta Astronaut 176 (2020) 531–541.

[5] K. Ishimura, K. Minesugi, T. Kawano, M. Ishida, K. Shoji, K. Abe, On orbit structural performance of hitomi (Astro-h), in: AIAA Scitech 2019 Forum, 2019, pp. 1–9.

[6] H. Awaki, H. Kunieda, M. Ishida, H. Matsumoto, A. Furuzawa, Y. Haba, T. Hayashi, R. Iizuka, K. Ishibashi, M. Itoh, T. Kosaka, Y. Maeda, I. Mitsuishi, T. Miyazawa, H. Mori, H. Nagano, Y. Namba, Y. Ogasaka, K. Ogi, T. Okajima, S. Sugita, Y. Suzuki, K. Tamura, Y. Tawara, K. Uesugi, S. Yamauchi, Performance of ASTRO-h hard x-ray telescope (HXT), in: Sp. Telesc. Instrum. 2016 Ultrav. to Gamma Ray, Vol. 9905, 2016, 990512.

[7] K. Nakazawa, G. Sato, M. Kokubun, T. Enoto, Y. Fukazawa, K. Hagino, K. Hayashi, J. Kataoka, J. Katsuta, S.B. Kobayashi, P. Laurent, F. Lebrun, O. Limousin, D. Maier, K. Makishima, T. Mizuno, K. Mori, T. Nakamori, Hard x-ray imager onboard Hitomi (ASTRO-H), J. Astron. Telesc. Instruments, Syst. 4 (2018) 1.

[8] K. Tamura, H. Astro-h, Supermirror design for hard X-ray telescopes on-board Hitomi (ASTRO-H), J. Astron. Telesc. Instrum. Syst. 4 (2018) 1.

[9] L. Sen Li, P.F. Qiang, L.Z. Sheng, Y.A. Liu, Z. Liu, D. Liu, B.S. Zhao, C.M. Zhang, Nested grazing incidence optics for x ray detection, Chinese Phys. B. 26 (2017) 1–5.

[10] N.J. Westergaard, D.D.M. Ferreira, S. Massahi, On X-ray telescopes in general and the Athena optics in particular, Nucl. Instrum. Methods Phys. Res. A 873 (2017) 5–11.

[11] K.D. Joensen, F.E. Christensen, H.W. Schnopper, J. Wood, K. Parker, O. Synthetic, M. Co, N.D. Troy, Medium-sized grazing incidence high-energy X-ray Telescopes employing continuously graded multilayers, 1736 (n.d.) pp. 239–248.

[12] Y. Tawara, K. Yamashita, Y. Ogasaka, K. Tamura, K. Haga, T. Okajima, S. Ichimaru, S. Takahashi, A. Gotou, H. Kitou, S. Fukuda, Y. Tsusaka, H. Kunieida, J. Tueller, P.J. Serlemitsos, Y. Soong, K.W. Chan, S.M. Owens, B. Barber, E. Dereniak, E.E. Young, A hard X-ray telescope with multilayered supermirrors for balloon observations of cosmic X-ray sources, Adv. Sp. Res. 30 (2002) 1313–1319.

[13] F. Mezei, Novel polarized neutron devices: supermirror and spin component amplifier, Commun. Phys. 1 (1976) 81–85.

[14] I.V. Kozhevnikov, I.N. Bukreeva, E. Ziegler, Design of X-ray supermirrors, Nucl. Instrum. Methods Phys. Res. A 460 (2001) 424–443.

[15] H. Li, S. Sakata, T. Johzaki, X. Tang, K. Matsuo, S. Lee, K.F. Farley Law, Y. Arikawa, Y. Ochiai, C. Liu, J. Nishibata, R. Takizawa, H. Morita, H. Azechi, YasuhikoSentoku, S. Fujioka, Enhanced relativistic electron beams intensity with self-generated resistive magnetic field, High Energy Density Phys. 36 (2020) 100773.

[16] Y. Li, T. Su, L. Sheng, P. Qiang, N. Xu, B. Zhao, X-ray transmittance characteristics and potential communication in re-enter plasma sheath, Optik (Stuttg) 197 (2019) 162917.

[17] X. Bin Cheng, Z.S. Wang, Z. Zhang, F. Wang, L. Chen, Design of X-ray super-mirrors using simulated annealing algorithm, Opt. Commun. 265 (2006) 197–206.

[18] A.M. Saxena, Characteristics of thin-film multilayer monochromator systems from ray-tracing calculations, Nucl. Instrum. Methods Phys. Res. A 454 (2000) 426–439.

[19] R. Tomaschitz, Effective partition function of crystals: Reconstruction from heat capacity data and Debye–Waller factor, Phys. B Condens. Matter. 593 (2020) 412243.

[20] E. Spiller, Reflective multilayer coatings for the far uv region, Appl. Opt. 15 (1976) 2333–2338.

[21] C.P. Jensen, F.E. Christensen, H.C. Chen, E.B.W. Smitt, E. Ziegler, Multilayer coating facility for the HEFT hard x-ray telescope, X-Ray Opt. Astron. Telesc. Multilayers Spectrom. Mission 4496 (2002) 104.

[22] S. Peng, Z. Liu, T. Sun, K. Wang, L. Yi, K. Yang, M. Chen, J. Wang, Simulation of transmitted X-rays in a polycapillary X-ray lens, Nucl. Instrum. Methods Phys. Res. A 795 (2015) 186–191.

[23] T.H. Lee, S.B. Hong, 8-channel CMOS low-noise fast readout circuits for CZT X-ray detectors, IEEE Trans. Nucl. Sci. 51 (2004) 821–825.

[24] B. Hussain, F. Che, C.P. Yue, L. Wu, Link budget analysis for visible light communication systems, in: 2015 IEEE Int. Wirel. Symp. IWS 2015, 2015.

[25] G. Zhang, C. Yu, C. Zhu, L. Liu, Feasibility study of multi-pixel photon counter serving as the detector in digital optical communications, Optik (Stuttg) 124 (2013) 5781–5786.